Global NEST Journal, Vol 26, No 4, 05443

Gap type effect on photocatalytic degradation using newly hydrotalcite nanoposite precursor synthesized by hydrothermal method

Souad Kerchich[1], Amel Boudjemaa[2], Redouane Chebout[2], Yacine Kerchich[3], Imane Béchohra[1]* and Khaldoun Bachari[2]

[1]Laboratoire de Génie de la réaction, Faculté de Génie mécanique et de Génie des procédés-Université des sciences et de la technologie Houari Boumediene (USTHB), B.P. 32, El Alia, Bab Ezzouar, 16111, Alger, Algérie.

[2]Centre De Recherche Scientifique Et Technique En Analyses Physico-Chimique (CRAPC), BP 384, Siège ex-Pasna Zone Industrielle, Bou-Ismail CP 42004, Tipaza, Algérie.

[3]Laboratoire des sciences et techniques de l'environnement, Ecole nationale polytechnique, BP 182, El Harrach, Alger, Algérie.

Received: 13/10/2023, Accepted: 08/04/2024, Available online: 15/04/2024

*to whom all correspondence should be addressed: e-mail: pchantzi@geo.auth.gr

https://doi.org/10.30955/gnj.005443

Graphical abstract

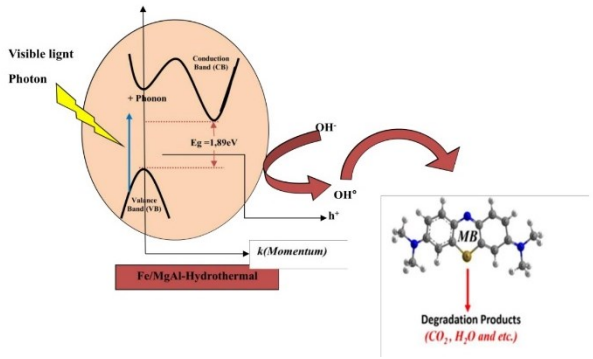

Abstract

A novel technique involving hydrothermal synthesis was employed to prepare nanocomposite precursors of lamellar double hydroxide based basic mixed oxides. This method extended ongoing research on iron-impregnated hydrotalcite-supported nanomaterials. The iron-based Fe/MgAl-h nanocomposite was prepared via dry impregnation, introducing a known % by weight of Fe $(NO_3)_3.9H_2O$ metal salt into the hydrothermally synthesized MgAl-h structure. For comparative analysis, the photocatalytic performance of Fe/MgAl-h was compared with the coprecipitation-synthesized Fe/MgAl-c after calcination at 400°C, using various characterization techniques. Structural examination revealed a double-layered hydroxyl structure and the presence of iron oxide phase Fe_2O_3 in Fe/MgAl-h400. Optical assessments indicated an indirect band gap energy of 1.89 eV for solid Fe/MgAl-h400, which is suitable for visible light absorption. Photocatalytic experiments for methylene blue (MB) dye degradation in aqueous solution were performed under artificial irradiation with a tungsten lamp as the visible light source, mirroring the conditions of Fe/MgAl-c400. Using 50 mg/L MB concentration and 0.5 g/L catalyst quantity, increased MB removal efficiency with time was observed. A comparative study of hydrothermal and coprecipitation synthesis methods showed decreased photodegradation for the hydrothermally prepared solid. Fe/MgAl-h400 and Fe/MgAl-c400 exhibited reaction efficiencies of approximately 46% and 67%, respectively, possibly attributed to their distinct indirect and direct band gap characteristics. Moreover, a wider band gap in a semiconductor material offers several advantages for the degradation of dyes.

Keywords: band gap, comparison, hydrothermal, co-precepitation, hydrotalcite, nanomaterials and photocatalysis

1. Introduction

Layered double hydroxides, also known as anionic clays or hydrotalcite-like compounds, are indeed a class of solid basic catalysts that have offer a promising platform for the development of environmentally friendly and efficient catalytic processes in the production of fine chemicals and other chemical transformations. Researchers continue to explore and optimize their properties for various applications in green chemistry and sustainable chemical synthesis.

hydrotalcites represent a category of both man-made and naturally occurring inorganic solids. These materials consist of two-dimensional layered structures composed of positively charged layers resembling brucite (Mg(OH)2). Within these layers, you'll find bivalent and trivalent metal ions arranged in an octahedral configuration (ALLMANN & HP 1969; Taylor 1973; Terzis *et al.* 1987; Pengfei *et al.* 2020).

The hydrotalcite's general formula, denoted as $[M_{1-x}^{2+}M_x^{3+}(OH)_2]^{x+}[A_{x/n}^{n-}\ mH_2O]^x$, encompasses various metal cations, represented by "M" including both divalent (e.g., Mg^{2+}, Zn^{2+}, Ni^{2+}, Co^{2+}, Ca^{2+} etc.) and trivalent (e.g., Al^{3+}, Fe^{3+},

Cr^{3+}, Mo^{3+}, Co^{3+}, Ga^{3+}etc.) species. Additionally, "A" represents the intercalated anions. These hydrotalcite layers maintain electrical neutrality by balancing their positive charge with the presence of negatively charged interlayer anions (Mishra *et al.* 2018b).

hydrotalcites, characterized by affordability, ready accessibility, and straightforward synthesis, have emerged as highly promising options for a range of applications. This is due to their extensive surface area, abundant surface-active sites, and impressive capacity for anion exchange, allowing them to incorporate anions of various sizes and types within their layers. With the significant attention hydrotalcites have garnered in recent years, a diverse array of hydrotalcite-based materials has been developed through specialized techniques or the incorporation of various metal cations to fulfill specific objectives (Fan *et al.* 2014; Peng *et al.* 2014; Patel *et al.* 2017; Arrabito *et al.* 2019; Yan *et al.* 2019; Ameena Shirin *et al.* 2021).

Over the past few decades, there has been a significant surge in interest surrounding the development of nanoparticle-scale technology for a wide range of applications. As a result, various synthesis techniques have emerged, encompassing gas phase, liquid phase, two-phase, sol-gel methods, co-precipitation, and hydrothermal methods (Miyata & Kumura 1973; Reichle 1985; Cavani *et al.* 1991; Sels *et al.* 2001). In this study, we aim to compare two prominent methods, namely the co-precipitation method, which involves maintaining both constant and variable pH levels (Crepaldi *et al.* 2000), and the hydrothermal method (Reichle 1986). It's worth noting that hydrothermal synthesis can be combined with co-precipitation to enhance the crystallization of hydrotalcite, a process with distinct advantages and limitations. Additionally, it's important to recognize that the synthesis method employed significantly influences the structure of LDH, with co-precipitation being a widely utilized approach in the production of hydrotalcite materials.

The precipitation at constant pH is generally applied to synthesize the hydrotalcites structure. The synthesis is carried out by the addition of the solution of two different metal salts dissolved in the distilled water. Which is added drop wise over an aqueous solution containing the mixture of anion to be intercalated and NaOH to accelerate coprecipitation reaction in the pH range .The reaction is carried out at room temperature (RT). The precipitate is then filtered and washed several times with distilled water. The drying temperature is not allowed to exceed 120 ^{o}C (Terzis *et al.* 1987). The use of this method leads to obtaining of pure and homogenous hydrotalcite with a high crystallinity. The advantage obtained by the co-precipitation at constant pH lies on the textural properties of the hydrotalcites materials. The hydrotalcites structure prepared by this method bears a small particle size, a high specific surface area and a high average pore diameter than the materials prepared at variable pH (Faour *et al.* 2010; Qin *et al.* 2020). On the other hand, the co-precipitation method allows to finely tuning the structure of the synthesized materials by controlling the MII/MIII molar ratios, type of interlayer anion, the synthesis time, temperature, and the pH (Thevenot *et al.* 1989; Zhao *et al.* 2003; Kloprogge *et al.* 2004; Klemkaite *et al.* 2011).

The hydrothermal synthesis is the combination with co-precipitation method to improve hydrotalcite crystallization, were consists of the treatment of fresh precipitate of co-precipitation synthesis resulting of mixing the solution containing metal salts and alkaline solution. The mixtures are usually put inside a Teflon-lined autoclave in the temperatures range from 80 to 350°C and the reaction times varied from hours to days (Miyata 1980). The advantages of this method include its simplicity and transformation of small crystallites of hydrotalcite into larger ones (Cavalcanti *et al.* 1987). The Mg-Al prepared by this method had hexagonally shaped crystallites with a lateral dimension of 1-3 µm (Xu & Lu 2005). This technique is recommended to prepare mixed metal oxides from hydrotalcite precursor (Xu & Lu 2005; Jing *et al.* 2010), ternary hydrotalcites systems and inorganic/organic hybrid hydrotalcite (Carja *et al.* 2008; Mishra *et al.* 2018a).

Recently, research on hydrotalcite has been directed towards the development of new hybrid or composite systems with improved physicochemical properties. The lamellar structures, in spite of their remarkable basic properties (Fan *et al.* 2014; Patel *et al.* 2017; Mishra *et al.* 2018b), are less used in catalytic reactions than the mixed oxides, which are easier to process and exhibit higher specific surface areas. Therefore, it will be very useful to adapt the basic properties of mixed oxides obtained from hydrotalcite precursors which will be synthesized by important methods like coprecipitation and hydrothermal method in order to carry out reactions requiring different basic resistances.

Numerous hydrotalcite supported nanoparticles, two-dimensional graphene oxide sheets or metal complexes have already proven to be very effective towards catalysis, photocatlysis, adsorption, sensing and biological applications (Choudary *et al.* 2002; Garcia-Gallastegui *et al.* 2012; Islam *et al.* 2015, 2019; Allou *et al.* 2017; Asif *et al.* 2017). Also, it is noteworthy that iron Oxide Nanoparticles supported on clays exhibit many interesting properties that can beused in a variety of applications (Oliveira *et al.* 2003; Nishio *et al.* 2007; da Silva *et al.* 2010; Chen *et al.* 2017; Kerchich *et al.* 2021).

In this article, Kerchich *et al.* (2021), conducted a study aiming to provide a systematic overview and a concise comparison between hydrothermal synthesis and co-precipitation methods. The research also includes a structural analysis and explores the potential application of Fe/MgAl in photocatalysis for the purpose of removing methylene blue dye.

2. Experimental section

2.1. Synthetic methods of semiconductor nanoparticles

2.1.1. Preparation of MgAl-h support by hydrothermal method

The MgAl support was prepared using two distinct methods. In the first method, known as the hydrothermal method, the reaction involved the addition of appropriate

quantities of Mg $(NO_3)_2.6H_2O$ (0.2 M, Aldrich, 99%), Al $(NO_3)_3.6H_2O$ (0.1 M, Aldrich, 99.1%), and NaOH (2 M, Aldrich, 99%) to achieve a constant pH of approximately 12. A laboratory pH meter (Hanna HI 2211) was employed to control the addition of the alkaline solution. The resulting mixture was placed inside a Teflon-lined autoclave and maintained at a temperature of 80°C for 17 hours (overnight). Subsequently, the formed gel underwent a washing process using distilled water and was finally dried overnight (Chebout *et al.* 2010; Kerchiche*et al.* 2017; Riman*et al.* 2002).

On the other hand, in the coprecipitation method used to synthesize MgAl-c material with the same Mg/Al, the initial step paralleled the hydrothermal method, involving the addition of the specified amounts of Mg $(NO_3)_2.6H_2O$ (0.2 M, Aldrich, 99%), Al $(NO_3)_3.6H_2O$ (0.1 M, Aldrich, 99.1%), and NaOH (2 M, Aldrich, 99%) to maintain a constant pH of around 12. The subsequent step diverged as the mixture was transferred to a balloon heater under nitrogen reflux, with the temperature maintained at 70°C for 18 hours to achieve a pure, well-crystallized compound. The final product was obtained after washing/centrifugation with bidistilled water and subsequent drying in an oven at 80°C for 12 hours (Riman *et al.* 2002; Chebout *et al.* 2010; Kerchiche *et al.* 2017). Finaly, both based HDL materials underwent a crushing and sieving process to achieve a fine particle size before before appropriate use. The host material resulting from the hydrothermal method was denoted as MgAl-LDHh, while the material synthesized through coprecipitation was designated as MgAl-LDHc.

2.1.2. Preparation of nanocomposite Fe_2O_3/MgAl-h

The protocol for preparing the Fe/MgAl solid by impregnation consists in bringing the MgAl support into contact with an iron content of a known % by weight of the metal precursor, the metal salt $Fe(NO_3)_3.9H_2O$ (Aldrich, 97%). For this work, the choice is focused on the dry impregnation method to prepare the Fe/ MgAl materials. The volume of the metal salt solution which must correspond to the volume of the pores of the support. This method is limited by the solubility of the precursor metal and is used to prepare catalysts with weak interactions between the metal and the support (Desportes *et al.* 2005). The mixture is then stirred for 2 hours by magnetic stirring and the excess solution is removed by evaporation then by drying in an oven overnight at 80°C and calcined at 400°C for 4 hours. The materials were denoted Fe/MgAl-h and Fe/MgAlc for hydrothermal and coprecipitation method respectly.

2.2. Characterization techniques

Diffuse reflectance infrared Fourier-transform (DRIFT) spectra of the samples were obtained using a Perkin-Elmer FTIR 1000 spectrometer, covering the wavelength range from 400 to 4000 cm^{-1}. The chemical composition of the materials was determined using a Rigaku “ZSX Primus II” X-Ray Fluorescence Spectrometer. Thermogravimetric (TGA) and differential thermal analysis (DTA) were conducted using a Thermal Analyzer (Model SDT Q 600-TA) instrument. The sample underwent heating from ambient temperature to 900°C under N2 flow, with a heating rate of 10°C min^{-1}. X-ray powder diffraction (XRD) patterns were recorded utilizing a Bruker D8 Advance X-ray diffractometer, employing Cu Kα1 radiation (λα = 1.54184 Å, 40 kV, and 50 mA). The data were collected within the 7° to 80° 2θ range. The structural characteristics of the materials were observed through scanning electron microscopy (SEM) using a FEI Quanta200 microscope operating at 20 kV. UV–vis diffuse reflectance (DRS) spectra were recorded using a Shimadzu model UV-2100 spectrophotometer equipped with an integrating sphere accessory, with BaSO4 serving as the reference material. The obtained reflectance (R%) from the DRS spectrum was utilized to determine the Eg value. The resulting solution was subject to analysis via atomic absorption spectroscopy (240-FS Fast Sequential, AA range from Agilent).

2.3. Photocatalytic reactivity study

To investigate the photocatalytic degradation of the dye, we followed a specific experimental procedure. This involved preparing a solution with a fixed concentration of the methylene blue (MB) and a known quantity of synthetic material. We conducted these experiments in a 500 mL Pyrex photochemical reactor with a double-wall design to maintain a constant temperature of 25°C, achieved by employing a temperature-controlled bath. The light source used for irradiation was a 200 W tungsten lamp emitting light in the range of 400–800 nm, with an intensity of 2.10×10^{19} photons per second. After the photocatalytic reaction, the suspension was subjected to centrifugation at 3000 rpm for 10 minutes. Subsequently, we filtered the suspension to eliminate any catalyst particles before performing absorbance measurements. To quantitatively assess the results, we measured the absorbance at the wavelength λmax = 665 nm using a Varian UV–visible Spectrophotometer (Cary 50 UV–vis Spectrophotometer).

3. Results and discussion

3.1. Structure and composition

All the synthesized hydrotalcites exhibited two-step decomposition upon heating under air (Figure 1). Initially, the first step was observed at temperatures ranging from 220 to 250°C, resulting in a 15% reduction in weight. This initial weight loss corresponded to the removal of interlamellar water molecules (Riman *et al.* 2002; Desportes *et al.* 2005; Kerchiche *et al.* 2017; Ramos-Ramírez *et al.* 2020). Subsequently, in the temperature range between 250 and 600°C, a weight loss of approximately 25% and 35% was observed for MgAl-h and Fe_2O_3/MgAl-h, respectively. These weight reductions were attributed to two processes: the decomposition of interlamellar carbonate and the dehydroxylation of the hydrotalcite sheets (Ramos-Ramírez *et al.* 2019). In this temperature range, the lamellar structure underwent distortion due to the formation of mixed oxides (Rey *et al.* 1992). This distortion led to the emergence of exothermic peaks at approximately 350 and 550°C, corresponding to the dehydroxylation of the brucite-like layers and the decomposition of incorporated anions, as explained by (Wang *et al.* 2007).

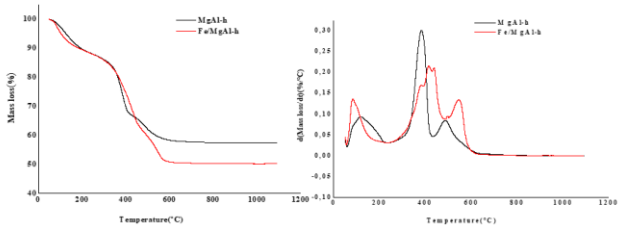

Figure 1. ATG/DTG of non-calcined MgAl-h and Fe/MgAl-h

The infrared spectra presented in Figure 2 for our samples exhibit typical characteristics associated with lamellar double hydroxides, consistent with findings from previous studies on hydrotalcites (Fernández *et al.* 1998; Das *et al.* 2002b; Ferreira *et al.* 2004). To know that the spectral characteristics of Fe/MgAl closely match those documented in prior literature, as evidenced by the findings of (Riman *et al.* 2002; Chebout *et al.* 2010; Mamat *et al.* 2014; Kerchiche *et al.* 2017). These spectra reveal similar vibration bands. Specifically, a broad band observed between 3450 - 3500 cm-1 is attributed to the presence of hydroxide groups (OH) within the layers and to intercalated and/or adsorbed water molecules. Another vibration band in the range of 1630-1640 cm-1 can be ascribed to the deformation of intercalated water molecules HOH (δHOH) (Leofanti *et al.* 1998).

The main bands associated with intercalated and adsorbed anions are observed within the 2000 to 1000 cm^{-1} range (Cavani *et al.* 1991). Furthermore, the remaining bands below 1000 cm^{-1} correspond to vibrations of M–O–M, which are characteristic of the double lamellar structure (Das *et al.* 2002b). Notably, a persistent vibration at 1450 cm^{-1}, observed in the material Fe/MgAl-h400, is indicative of the presence of maghemite iron oxide (γ-Fe_2O_3). In Figure 2, it is evident that the peak intensities related to water dehydration and dehydroxylation decrease, a phenomenon attributed to the calcination of the materials at 400°C(Barakat 2012; Kerchich *et al.* 2021).

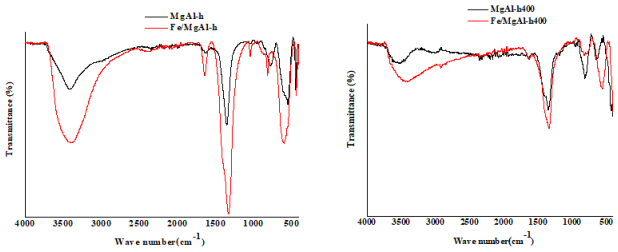

Figure 2. FTIR spectra of the not calcined MgAl-h and calcined Fe/MgAl-h400

the elemental analyses of the samples are reported in Table 1, shown that the experimental molar ratios M^{2+}/M^{3+} are in good agreement with the theoretical values (M^{2+}/M^{3+} = 2). On the other hand, $M^{3+}/(M^{2++}\ M^{3+})$ values are between 0.31 and 0.32, these values correspond to the optimal ratios necessary for achieving a well-formed crystalline LDH structure (Miyata 1983; Fernández *et al.* 1998; Leofanti *et al.* 1998; Das *et al.* 2002a; Barakat 2012; Mamat *et al.* 2014).

Table 1. Chemical analysis and band gap energies of MgAl-h, Fe/MgAl-h and Fe/MgAl-c materials calcined at 400°C

Samples	T°C	Formulas	$(M^{2+}/M^{3+})_{theo}$	$(M^{2+}/M^{3+})_{exp}$	$x = M^{3+}/(M^{2++}\ M^{3+})$	% Fe	Eg (eV)
MgAl-h	400	$Mg_{0.68}Al_{0.32}$-h	2	2.1	0.32	-	-
Fe_2O_3/MgAl-h	400	Fe/$Mg_{0.69}Al_{0.31}$-h	2	2.22	0.31	7.73	1.89
Fe_2O_3/MgAl-c	400	Fe/$Mg_{0.68}Al_{0.32}$-c	2	2.06	0.32	9.73	2.02

The X-ray diffraction (XRD) patterns presented in Figure 3 offer valuable insights into the samples we prepared. These patterns exhibit distinctive characteristics for various samples, such as non-calcined samples Mg-Al-h and Mg-Al-c, as well as calcined samples such as Mg-Al-h400, Mg-Al-c400, Fe/Mg-Al-h400, and Fe/Mg-Al-c400. Notably, these patterns reveal prominent diffraction peaks at specific 2θ values (11.87, 23.75, 34.76, 39.1, 46.49, 61.12, 62.26, 66.32, 72.48, and 75.08°) corresponding to the (003), (006), (009), (012), (018), (110), and (113) planes. These peaks unequivocally confirm the presence of the MgAl structure, consistent with data from PDF-#38-0487, which describes a rhombohedral structure (Chen & Qu 2003; Lakraimi *et al.* 2006; Hong *et al.* 2014). However, it's important to note that the absence of peaks corresponding to (003) and (006) after heat treatment indicates the disintegration of the hydrotalcites lamellar structure, aligning with previous research findings (Chebout *et al.* 2010; Kerchiche *et al.* 2017; Ramos-Ramírez *et al.* 2020). This transformation suggests a shift from the hydrotalcite structure to oxides. Remarkably, new peaks emerge at 2θ values of 31.74, 35.35, 42.91, 62.40, 74.89, and 78.60°, indicating the presence of MgO (JCPDS No. 87-0653). In contrast, for Fe/MgAl, diffraction peaks appear at 2θ values of 22.9, 29.1, 31.6, 39.0, 48.3, 55.6, and 56.6°, clearly indicating the presence of iron oxide in the γ-phase (γ-Fe2O3, maghemite). The corresponding interlayer spacing (d003), approximately 0.8 nm for all three samples, is consistent with a Mg/Al molar ratio close to 2 in the brucite-like layers and the presence of carbonate as charge compensating anions, as reported in previous studies (Wang *et al.* 2007; Chebout *et al.* 2010; Kerchiche *et al.* 2017).

The "a" parameter, representing the average metal-to-metal distance within the layers and determined from the (110) diffraction line, was found to be 0.3 nm for the MgAl sample and 0.2 nm for the Fe/MgAl sample. This observation substantiates the alteration in the composition of hydrotalcite layers in the presence of Fe^{3+}. These computed values align closely with those documented in previous studies (Millange *et al.* 2000; Chebout *et al.* 2010; León *et al.* 2010; Kerchiche *et al.* 2017).

The size of crystallite particles (D) was calculated using the Debye-Scherrer equation (Tichit *et al.* 2006). For MgAl-h400, Fe/MgAl-h400, and Fe/MgAl-c400, the calculated D values are approximately 2.1 nm, 3.8 nm, and 3.5 nm, respectively. These results indicate an increase in particle size due to the presence of iron content, as demonstrated

in the work by (Kerchich *et al.* 2021). Furthermore, it is worth noting that the hydrothermal preparation method for Mg-Al confirmed an enhancement in crystallinity.

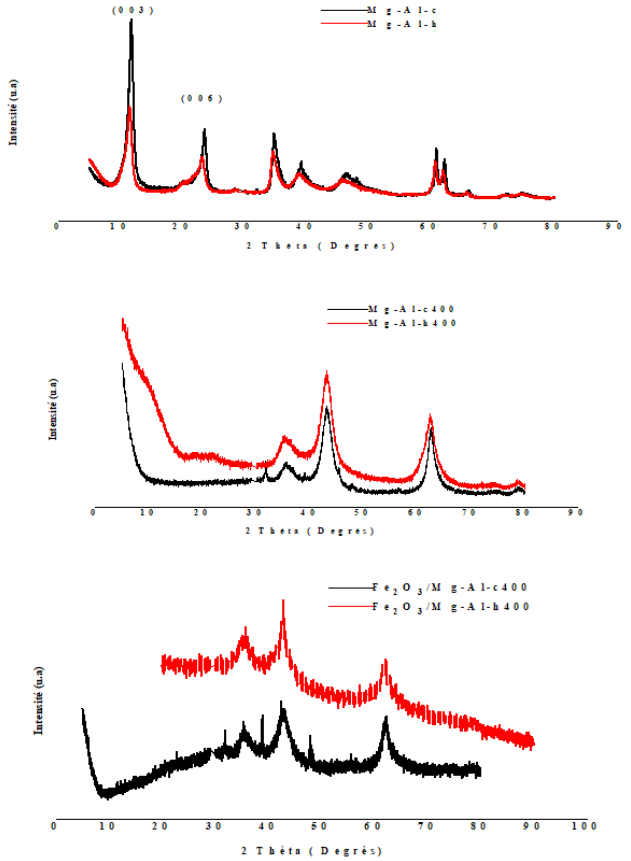

Figure 3. XRD patterns of (a) MgAl-h, MgAL-c, (b) MgAl-h400, MgAl-c400 and (c) Fe/MgAl-h400, Fe/MgAl-c400

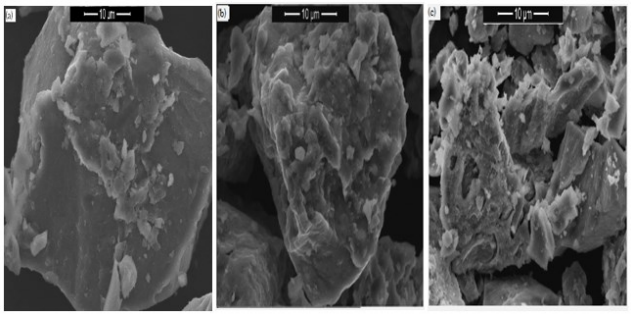

Figure 4. SEM images: (a) MgAl-h, (b) Fe/MgAl-h400 and (c) Fe/MgAl-c400

The SEM micrograph in Figure 4a reveals that the hydrothermal method yielded a synthetic MgAl-h material exhibiting a plate-like structure characteristic of lamellar phases. Upon calcination, as depicted in the micrographs in Figure 4b and 4c, it becomes evident that the material exhibits enhanced crystallinity and an increase in particle size when compared to the hydrothermal method. Additionally, the surface of the hydrotalcite is conspicuously adorned with uniformly dispersed iron oxide nanoparticles, creating a relatively homogeneous appearance of γ-Fe2O3 (Barakat 2012; Kerchich *et al.* 2021).

Hence, an increase in the cristallinty signifies a reduction in the bandgap width, a concept supported by various studies (Burstein 1954; Moss 1954; Aliahmad & Nasiri Moghaddam 2013). This relationship is corroborated by our assessment of the bandgap (Eg) in our samples using Tauc's equation (Tauc *et al.* 1966), expressed as:

$$(\alpha h\upsilon)m = B\,(h\upsilon - Eg) \qquad (1)$$

In this equation, B represents a constant, Eg denotes the optical gap energy, α stands for the optical absorption coefficient, hv represents the energy of the photon, h is the Planck constant, and v signifies photon frequency. The value of Eg is determined by plotting $(\alpha h\upsilon)^m$ against (hυ) and extrapolating the linear portion of the curve that intersects the energy axis hυ. For direct gap materials, this corresponds to m = 2, whereas for indirect gap materials, it's m = 1/2.

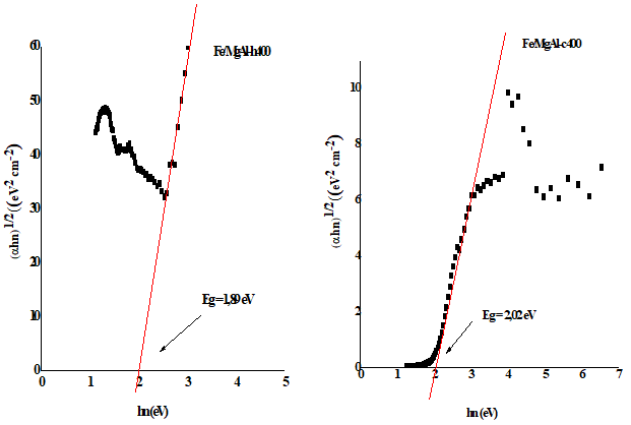

Figure 5. Band gap energies of calcined Fe/MgAl-h400 and Fe/MgAl-c400

Fe/MgAl-h400 exhibited an indirect band gap energy with a value of 1.89 eV, compared to Fe/MgAl-c400 exhibited a direct band gap energy with a value of 2.02 (Figure 5). Thus, the band gap values of synthesis materials are slightly lower than that of the bulk Fe_2O_3 (2.1 eV). This widening of the prohibited band is an effect of the quantum confinement observed in many other synthesized semiconductor materials (Wen *et al.* 2005; Bepari *et al.* 2017). So, such narrow band gap is beneficial for the efficient utilization of visible light (Iron oxide exhibits a red color, which can absorb in the visible region). The narrower band gap of the material can harvest more photons to excite the e- from the valence band (VB) to the conduction band (CB) and thus, the photocatalytic activity is increased.

3.2. Gap type effect on photocatalytic degradation by Fe/MgAl- photocatalyst

The photocatalytic activity of the synthesized Fe/MgAl-h400 material was evaluated for the degradation of MB dye in aqueous solution. The tests examined with the hydrothermal method under artificial irradiation using a tungsten lamp as visible light, under the same conditions which are applied for the evolution of the catalytic activity of the Fe/MgAl-c400 material prepared by the coprecipitation method. Namely, the mass percentage of iron, the dye concentration, the amount of photocatalyst, the temperature of calcinations and at a free pH (5.9). Using MB concentration of 50 mg/L and a catalyst amount of 0,5 g/L, it is can be easily observed that MB removal increased efficiency with the reaction time (Figure 6). The

yield obtained from the degradation of MB is as expected due to the presence of iron oxide with a maghemite structure (γ-Fe_2O_3) (Kerchich *et al.* 2021), that is a semiconductor generally known for its visible band gap energy (~ 2.1 eV). So, the supported catalysts on an inert support as hydrotalcite structure increase the metal dispersion, and the photo-activity depended particularly on the particle (Boudjemaa *et al.* 2009; Boudjemaa & Trari 2010). According to the data shown in Figure 6, the highest reactivity is observed with with the photocatalyst prepared by the Fe/MgAl-c400 coprecipitation. After 240 min of irradiation the reaction efficiency is around of 67 and 46% for Fe/MgAl-c400 and Fe/MgAl-h400 photocatalysts, respectively.

To compare the performance of two synthesis methods, hydrothermal and coprecipitation, in the context of photodegradation, the results clearly indicate that MgAl-h400 exhibits lower photodegradation. Despite their impressive fundamental properties as adsorbents, lamellar structures are less frequently employed in photocatalytic reactions (Figueras 2004; Figueras *et al.* 2006). Photocatalysis operates on the principle of degrading materials under the influence of light with energy equal to or greater than its band gap ($h\upsilon \geq Eg$). This process involves catalyzing chemical reactions through electronically excited species generated by photon absorption (Khatamian *et al.* 2010; Dessie 2017; Terna *et al.* 2021).

When the material is irradiated with a photon with energy greater than or equal to the band gap (Eg), it results in the generation of an electron-hole pair (e^-/h^+), leading to the formation of hydroxyl radicals (OH°) and superoxide anion radicals ($O_2^{\circ-}$), as well as the photogenerated hole (h^+) responsible for the degradation of organic molecules. Under irradiation, the h+ hole reacts with water to produce OH° radicals. It has been previously demonstrated by (Kerchich *et al.* 2021), that OH° radicals and h^+ holes are the reactive species involved in the photodegradation of MB (methylene blue) for Fe/MgAl-400 materials. A photocatalysis goes beyond the adsorption property of solids (adsorbents) to capture certain adsorbates on their surfaces, therefore does not is not just based on the property that solids have of fixing certain adsorbates on their surface. Hence, based on the gap results, we can conclude that the main difference in lies in the direct and indirect band gaps exhibited by the Fe/MgAl-c400 and Fe/MgAl-h400 semiconductors, respectively.

The fundamental distinction between direct and indirect band gaps lies in their crystal momentum characteristics. In a direct band gap semiconductor, both electrons and holes possess identical crystal momentum values in the conduction and valence bands, enabling direct photon emission by an electron. Conversely, indirect band gap semiconductors lack this symmetry, making it impossible for an electron to directly emit a photon since photons cannot carry crystal momentum. For radiative recombination to take place in an indirect band gap material, it necessitates the involvement of phonon absorption or emission, where the phonon's momentum compensates for the difference between the electron and hole momenta. However, this process occurs at a considerably slower pace because it relies on the intersection of three entities: an electron, a photon, and a phonon. As a result, the recombination process is significantly more efficient in direct band gap semiconductors compared to indirect band gap semiconductors. In the case of indirect band gap semiconductors, the recombination process relies on phonon mediation, which results in a lower photocatalytic efficiency compared to direct band gap semiconductors (Johari & Shenoy 2012; Conley *et al.* 2013; Gabal *et al.* 2023). In conclusion, a wider band gap increases the density of electronic states in the material. This means that there are more sites available for chemical reactions, which can facilitate the degradation of dyes. Excited electrons from the valence band can more easily interact with other molecules and chemically react to degrade the dyes.

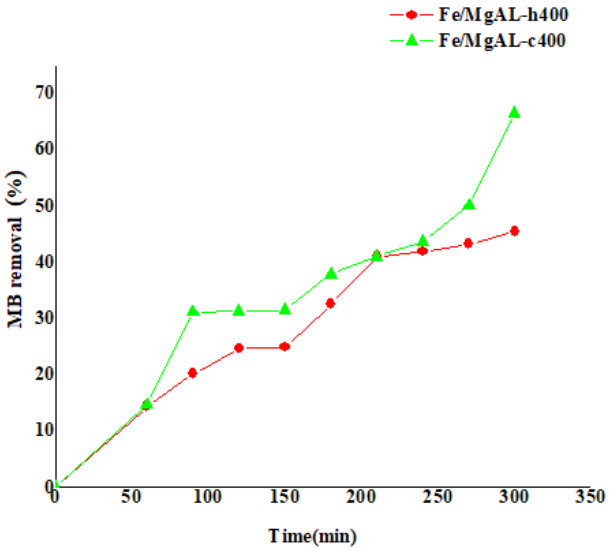

Figure 6. Effect of the synthesis method on the removal of MB (50ppm BM, 0.5g/l mass photocatalys, free pH (5,9))

4. Conclusion

The research presented in this article contributes to the advancement of knowledge by focusing on the development of novel photocatalysts based on iron oxide within the lamellar double hydroxide structure, and their application in environmental contexts. Hydrotalcite-based materials have garnered significant interest in recent decades due to their simple synthesis processes and wide range of applications. These materials are predominantly synthesized through co-precipitation and hydrothermal methods, enabling the combination of M(II) and M(III) cations along with interlayer anions within the hydrotalcite structure. The unique structural properties of hydrotalcite make it a promising candidate for various applications, particularly in the field of photocatalysis.

This study successfully demonstrated the effectiveness of the hydrothermal method in synthesizing a new photocatalyst, Fe/MgAl-h400, based on iron. The key findings of the research are as follows:

The Fe/MgAl-h400 photocatalyst was synthesized using the impregnation method and underwent comprehensive

physico-chemical characterization, including XRF, XRD, SEM, ATG/DSC, RDs, and FTIR techniques.

The infrared spectra exhibited typical characteristics associated with lamellar double hydroxides, consistent with previous studies on hydrotalcites, and the XRD results clearly indicated the presence of iron oxide.

The Fe/MgAl-h400 photocatalyst demonstrated improved crystallinity and remarkable photoactivity under visible light. After 240 minutes of irradiation, the Fe/MgAl-h400 photocatalyst, with a particle size of approximately 3.8 nm and an indirect bandgap energy of 1.89 eV, exhibited a notable photodegradation rate of approximately 46%.

The Fe/MgAl-h400 semiconductor, with an indirect bandgap, undergoes a recombination process that depends on phonon mediation, leading to lower photocatalytic efficiency compared to direct bandgap semiconductors. However, a wider bandgap in semiconductor materials provides notable advantages for dye degradation, including enhanced light absorption, increased reactivity with dyes, greater stability, and improved durability.

Therefore, enhancing the qualities and modifying the basic properties of mixed oxides derived from hydrotalcite precursors is highly beneficial. These modifications facilitate reactions that require varying basic strength and contribute to more efficient and controlled degradation of dyes, which is crucial in fields such as wastewater treatment, air purification, and the removal of unwanted dyes.

References

Aliahmad M. and Nasiri Moghaddam N. (2013). Synthesis of maghemite (γ-Fe_2O_3) nanoparticles by thermal-decomposition of magnetite (Fe3O4) nanoparticles. *Materials Science-Poland*, **31**, 264–268.

Allmann R. and Hp J. (1969). *DIE STRUKTUR DES HYDROTALKITS.*, Neues Jahrb Mineral Monatsh.

Allou N. B., Saikia P., Borah A. and Goswamee R.L. (2017). Hybrid nanocomposites of layered double hydroxides: an update of their biological applications and future prospects. *Colloid and Polymer Science*, **295**, 725–747.

Ameena Shirin V.K., Sankar R., Johnson A.P., Gangadharappa H.V. and Pramod K. (2021). Advanced drug delivery applications of layered double hydroxide. *Journal of Controlled Release*, **330**, 398–426.

Arrabito G., Bonasera A., Prestopino G., Orsini A., Mattoccia A., Martinelli E., Pignataro B. and Medaglia P.G. (2019). Layered Double Hydroxides: A Toolbox for Chemistry and Biology. *Crystals*, **9**, 361.

Asif M., Haitao W., Shuang D., Aziz A., Zhang G., Xiao F. and Liu H. (2017). Metal oxide intercalated layered double hydroxide nanosphere: With enhanced electrocatalyic activity towards H2O2 for biological applications. *Sensors and Actuators B: Chemical*, **239**, 243–252.

Barakat N.A.M. (2012). Synthesis and characterization of maghemite iron oxide (γ-Fe_2O_3) nanofibers: novel semiconductor with magnetic feature. *Journal of Materials Science*, **47**, 6237–6245.

Bepari R.A., Bharali P. and Das B.K. (2017). Controlled synthesis of α- and γ-Fe2O3 nanoparticles via thermolysis of PVA gels and studies on α-Fe2O3 catalyzed styrene epoxidation. *Journal of Saudi Chemical Society*, **S1**, S170–S178.

Boudjemaa A. and Trari M. (2010). Photo-catalytic hydrogen production over Fe2O3 based catalysts. *International Journal of Hydrogen Energy*, **35**, 7684–7689.

Boudjemaa A., Boumaza S., Trari M., Bouarab R. and Bouguelia A. (2009). Physical and photo-electrochemical characterizations of α-Fe2O3. Application for hydrogen production. *International Journal of Hydrogen Energy*, **34**, 4268–4274.

Burstein E. (1954). Anomalous Optical Absorption Limit in InSb. *Physical Review*, **93**, 632–633.

Carja G., Chitanu G.C., Kameshima Y., Chiriac H. and Okada K. (2008). LDH–maleic anhydride copolymers as new hybrid materials and their textural organisation. *Applied Clay Science*, **41**, 107–112.

Cavalcanti F.A.P., Schutz A. and Biloen P. (1987). *Interlayer Accessibility in Layered Double-Metal Hydroxides*. *Studies in Surface Science and Catalysis* Preparation of Catalysts IV. (ed. by B. Delmon), P. Grange), P. A. Jacobs), and G. Poncelet), pp. 165–174. Elsevier.

Cavani F., Trifirò F. and Vaccari A. (1991). Hydrotalcite-type anionic clays: Preparation, properties and applications. *Catalysis Today*, **11**, 173–301.

Chebout R., Tichit D., Layrac G., Barama A., Coq B., Cota I., Rangel E. R. and Medina F. (2010). New basic catalysts obtained from layered double hydroxides nanocomposites. *Solid State Sciences*, **12**, 1013–1017.

Chen M., Hou C., Huo D., Fa H., Zhao Y. and Shen C. (2017). A sensitive electrochemical DNA biosensor based on three-dimensional nitrogen-doped graphene and Fe3O4 nanoparticles. *Sensors and Actuators B: Chemical*, **239**, 421–429.

Chen W. and Qu B. (2003). Structural Characteristics and Thermal Properties of PE-g-MA/MgAl-LDH Exfoliation Nanocomposites Synthesized by Solution Intercalation. *Chemistry of Materials*, **15**, 3208–3213.

Choudary B.M., Madhi S., Chowdari N.S., Kantam M.L. and Sreedhar B. (2002). Layered Double Hydroxide Supported Nanopalladium Catalyst for Heck-, Suzuki-, Sonogashira-, and Stille-Type Coupling Reactions of Chloroarenes. *Journal of the American Chemical Society*, **124**, 14127–14136.

Conley H.J., Wang B., Ziegler J.I., Haglund R.F., Pantelides S.T. and Bolotin K.I. (2013). Bandgap engineering of strained monolayer and bilayer MoS2. *Nano Letters*, **13**, 3626–3630.

Crepaldi E.L., Pavan P.C. and Valim J.B. (2000). Anion exchange in layered double hydroxides by surfactant salt formation. *Journal of Materials Chemistry*, **10**, 1337–1343.

da Silva D.C., Neto K.S., Coaquira J.A.H., Araujo P.P., Cintra D.O.S., Lima E.C.D., Guilherme L.R., Mosiniewicz-Szablewska E. and Morais P.C. (2010). Magnetic characterization of vermiculite-based magnetic nanocomposites. *Journal of Non-Crystalline Solids*, **356**, 2574–2577.

Das J., Das D., Dash G.P. and Parida K.M. (2002a). Studies on Mg/Fe hydrotalcite-like-compound (HTlc) I. Removal of inorganic selenite (SeO3(2-)) from aqueous medium. *Journal of Colloid and Interface Science*, **251**, 26–32.

Das J., Das D., Dash G.P. and Parida K.M. (2002b). Studies on Mg/Fe Hydrotalcite-Like-Compound (HTlc): I. Removal of

Inorganic Selenite (SeO32−) from Aqueous Medium. *Journal of Colloid and Interface Science*, **251**, 26–32.

Desportes S., Steinmetz D., Hémati M., Philippot K. and Chaudret B. (2005). Production of supported asymmetric catalysts in a fluidised bed. *Powder Technology*, **157**, 12–19.

Dessie Y. (2017). Optical Photocatalytic Degradation of Methylene Blue Using Lignocellulose Modified TiO2. *American Journal of Optics and Photonics*, **5**, 55.

Fan G., Li F., Evans D. G. and Duan X. (2014). Catalytic applications of layered double hydroxides: recent advances and perspectives. *Chemical Society Reviews*, **43**, 7040–7066.

Faour A., Prévot V. and Taviot-Gueho C. (2010). Microstructural study of different LDH morphologies obtained via different synthesis routes. *Journal of Physics and Chemistry of Solids*, **71**, 487–490.

Fernández J.M., Ulibarri M.A., Labajos F.M. and Rives V. (1998). The effect of iron on the crystalline phases formed upon thermal decomposition of Mg-Al-Fe hydrotalcites. *Journal of Materials Chemistry*, **8**, 2507–2514.

Ferreira O.P., Alves O.L., Gouveia D.X., Souza Filho A.G., de Paiva J.A.C. and Filho J.M. (2004). Thermal decomposition and structural reconstruction effect on Mg–Fe-based hydrotalcite compounds. *Journal of Solid State Chemistry*, **177**, 3058–3069.

Figueras F. (2004). Base Catalysis in the Synthesis of Fine Chemicals. *Topics in Catalysis*, **29**, 189–196.

Figueras F., Kantam M.L. and Choudary B.M. (2006). Solid Base Catalysts in Organic Synthesis. *Current Organic Chemistry*, **10**, 1627–1637.

Gabal M.A., Al-Harthy E.A., Al Angari Y.M., Awad A., Al-Juaid A.A. and Saeed A. (2023). Synthesis, characterization and electrical properties of polypyrrole/Mn0.8Zn0.2Fe2O4/GO ternary hybrid composites using spent Zn-C batteries. *Journal of Sol-Gel Science and Technology*, **105**, 781–792.

Garcia-Gallastegui A., Iruretagoyena D., Gouvea V., Mokhtar M., Asiri A.M., Basahel S.N., Al-Thabaiti S.A., Alyoubi A.O., Chadwick D. and Shaffer M.S.P. (2012). Graphene Oxide as Support for Layered Double Hydroxides: Enhancing the CO2 Adsorption Capacity. *Chemistry of Materials*, **24**, 4531–4539.

Hong J., Zhang W., Wang Y., Zhou T. and Xu R. (2014). Photocatalytic Reduction of Carbon Dioxide over Self-Assembled Carbon Nitride and Layered Double Hydroxide: The Role of Carbon Dioxide Enrichment. *ChemCatChem*, **6**, 2315–2321.

Islam D.A., Barman K., Jasimuddin S. and Acharya H. (2019). Synthesis of ultrasmall and monodisperse sulfur nanoparticle intercalated CoAl layered double hydroxide and its electro-catalytic water oxidation reaction at neutral pH. *Nanoscale*, **11**, 7560–7566.

Islam D.A., Borah D. and Acharya H. (2015). Controlled synthesis of monodisperse silver nanoparticles supported layered double hydroxide catalyst. *RSC Advances*, **5**, 13239–13245.

Jing F., Zhang Y., Luo S., Chu W. and Qian W. (2010). Nano-size MZnAl (M=Cu, Co, Ni) metal oxides obtained by combining hydrothermal synthesis with urea homogeneous precipitation procedures. *Applied Clay Science*, **48**, 203–207.

Johari P. and Shenoy V.B. (2012). Tuning the Electronic Properties of Semiconducting Transition Metal Dichalcogenides by Applying Mechanical Strains. *ACS Nano*, **6**, 5449–5456.

Kerchich S., Boudjemaa A., Chebout R., Bachari K. and Mameri N. (2021). High performance of δ-Fe2O3 novel photo-catalyst supported on LDH structure. *Journal of Photochemistry and Photobiology A: Chemistry*, **406**, 113001.

Kerchiche S., Chebout R., Barama A. and Bachari K. (2017) New way for iron introduction in LDH matrix used as catalysts for Friedel–Crafts reactions. *Arabian Journal of Chemistry*, **10**, S328–S333.

Khatamian M., Daneshvar N. and Sabaee S. (2010) Heterogeneos Photocatalytic Decolorization of Brown NG by TiO2 –UV Process. *Iranian Journal of Chemistry and Chemical Engineering*, **29**, 19–26.

Klemkaite K., Prosycevas I., Taraskevicius R., Khinsky A. and Kareiva A. (2011). Synthesis and characterization of layered double hydroxides with different cations (Mg, Co, Ni, Al), decomposition and reformation of mixed metal oxides to layered structures. *Open Chemistry*, **9**, 275–282.

Kloprogge J.T., Hickey L. and Frost R.L. (2004). The effects of synthesis pH and hydrothermal treatment on the formation of zinc aluminum hydrotalcites. *Journal of Solid State Chemistry*, **177**, 4047–4057.

Lakraimi M., Legrouri A., Barroug A., De Roy A. and Besse J.P. (2006). Synthesis and characterisation of a new stable organo-mineral hybrid nanomaterial: 4-Chlorobenzenesulfonate in the zinc–aluminium layered double hydroxide. *Materials Research Bulletin*, **41**, 1763–1774.

Leofanti G., Padovan M., Tozzola G. and Venturelli B. (1998). Surface area and pore texture of catalysts. *Catalysis Today*, **41**, 207–219.

León M., Díaz E., Bennici S., Vega A., Ordóñez S. and Auroux A. (2010). Adsorption of CO2 on Hydrotalcite-Derived Mixed Oxides: Sorption Mechanisms and Consequences for Adsorption Irreversibility. *Industrial & Engineering Chemistry Research*, **49**, 3663–3671.

Mamat M., Tagg T., Khairul W.M., Abdullah M.A.A., Tahir N.M., Jubri Z. and As'ari R.A. (2014). Behavior of Layered Double Hydroxides Having Different Divalent Transition Metal Groups. *Applied Mechanics and Materials*, **563**, 94–101.

Millange F., Walton R.I. and O'Hare D. (2000). Time-resolved in situ X-ray diffraction study of the liquid-phase reconstruction of Mg–Al–carbonate hydrotalcite-like compounds. *Journal of Materials Chemistry*, **10**, 1713–1720.

Mishra G., Dash B. and Pandey S. (2018a). Layered double hydroxides: A brief review from fundamentals to application as evolving biomaterials. *Applied Clay Science*, **153**, 172–186.

Mishra G., Dash B., Pandey S. and Sethi D. (2018b). Ternary layered double hydroxides (LDH) based on Cu- substituted ZnAl for the design of efficient antibacterial ceramics. *Applied Clay Science*, **165**, 214–222.

Miyata S. (1980). Physico-Chemical Properties of Synthetic Hydrotalcites in Relation to Composition. *Clays and Clay Minerals*, **28**, 50–56.

Miyata S. (1983). Anion-Exchange Properties of Hydrotalcite-Like Compounds. *Clays and Clay Minerals*, **31**, 305–311.

Miyata S. and Kumura T. (1973). Synthesis of new hydrotalcite-like compounds and their physico-chemical properties. *Chemistry Letters*, **2**, 843–848.

Moss T.S. (1954). The Interpretation of the Properties of Indium Antimonide. *Proceedings of the Physical Society. Section B*, **67**, 775.

Nishio K., Ikeda M., Gokon N., Tsubouchi S., Narimatsu H., Mochizuki Y., Sakamoto S., Sandhu A., Abe M. and Handa H. (2007). Preparation of size-controlled (30–100nm) magnetite nanoparticles for biomedical applications. *Journal of Magnetism and Magnetic Materials*, **310**, 2408–2410.

Oliveira L.C.A., Rios R.V.R.A., Fabris J.D., Sapag K., Garg V.K. and Lago R.M. (2003). Clay–iron oxide magnetic composites for the adsorption of contaminants in water. *Applied Clay Science*, **22**, 169–177.

Patel R., Park J.T., Patel M., Dash J.K., Gowd E.B., Karpoormath R., Mishra A., Kwak J. and Kim J.H. (2017). Transition-metal-based layered double hydroxides tailored for energy conversion and storage. *Journal of Materials Chemistry A*, **6**, 12–29.

Peng F., Luo T. and Yuan Y. (2014). Controllable synthesis of Mg–Fe layered double hydroxide nanoplates with specific Mg/Fe ratios and their effect on adsorption of As (V) from water. *New Journal of Chemistry*, **38**, 4427–4433.

Pengfei Y., Yuanxin X., Na Y. and Yong A. (2020). Preparation of Uniform Highly Dispersed Mg–Al-LDHs and Their Adsorption Performance for Chloride Ions. *Industrial & Engineering Chemistry Research*, **59**, 10697–10704.

Qin Y., Zhao R. and Bai C. (2020). Layered double hydroxide-oriented assembly by negatively charged graphene oxide for NO2 sensing at ppb level. *New Journal of Chemistry*, **44**, 16985–16994.

Ramos-Ramírez E., Gutiérrez-Ortega N. L., Tzompantzi-Morales F., Barrera-Rodríguez A., Castillo-Rodríguez J.C., Tzompantzi-Flores C., Santolalla-Vargas C.E. and Guevara-Hornedo M. del P. (2020). Photocatalytic Degradation of 2,4-Dichlorophenol on NiAl-Mixed Oxides Derivatives of Activated Layered Double Hydroxides. *Topics in Catalysis*, **63**, 546–563.

Ramos-Ramírez E., Tzompantzi-Morales F., Gutiérrez-Ortega N., Mojica-Calvillo H. G. and Castillo-Rodríguez J. (2019). Photocatalytic Degradation of 2,4,6-Trichlorophenol by MgO–MgFe2O4 Derived from Layered Double Hydroxide Structures. *Catalysts*, **9**, 454.

Reichle W. T. (1985). Catalytic reactions by thermally activated, synthetic, anionic clay minerals. *Journal of Catalysis*, **94**, 547–557.

Reichle W.T. (1986). Synthesis of anionic clay minerals (mixed metal hydroxides, hydrotalcite). *Solid State Ionics*, **22**, 135–141.

Rey F., Fornés V. and Rojo J.M. (1992). Thermal decomposition of hydrotalcites. An infrared and nuclear magnetic resonance spectroscopic study. *Journal of the Chemical Society, Faraday Transactions*, **88**, 2233–2238.

Riman R.E., Suchanek W.L. and Lencka M.M. (2002). Hydrothermal crystallization of ceramics. *Annales de Chimie Science des Matériaux*, **27**, 15–36.

Sels B.F., De Vos D.E. and Jacobs P.A. (2001). Hydrotalcite-like anionic clays in catalytic organic reactions. *Catalysis Reviews*, **43**, 443–488.

Tauc J., Grigorovici R. and Vancu A. (1966). Optical Properties and Electronic Structure of Amorphous Germanium. *physica status solidi (b)*, **15**, 627–637.

Taylor H.F.W. (1973). Crystal structures of some double hydroxide minerals. *Mineralogical magazine*, **39**, 377–389.

Terna A.D., Elemike E.E., Mbonu J.I., Osafile O.E. and Ezeani R.O. (2021). The future of semiconductors nanoparticles: Synthesis, properties and applications. *Materials Science and Engineering: B*, **272**, 115363.

Terzis A., Filippakis S., Kuzel H.-J. and Burzlaff H. (1987). The crystal structure of Ca2Al (OH)6Cl $2H_2O$. *Zeitschrift für Kristallographie - Crystalline Materials*, **181**, 29–34.

Thevenot F., Szymanski R. and Chaumette P. (1989). Preparation and Characterization of Al-Rich Zn-Al Hydrotalcite-Like Compounds. *Clays and Clay Minerals*, **37**, 396–402.

Tichit D., Iborra S., Corma A. and Brunel D. (2006). *Base-Type Catalysis*. *Catalysts for Fine Chemical Synthesis*, pp. 171–205. John Wiley & Sons, Ltd.

Wang L.-Y., Wu G.-Q. and Evans D.G. (2007). Synthesis and characterization of a layered double hydroxide containing an intercalated nickel (II) citrate complex. *Materials Chemistry and Physics*, **104**, 133–140.

Wen X., Wang S., Ding Y., Wang Z. L. and Yang S. (2005). Controlled Growth of Large-Area, Uniform, Vertically Aligned Arrays of α-Fe2O3 Nanobelts and Nanowires. *The Journal of Physical Chemistry B*, **109**, 215–220.

Xu Z.P. and Lu G.Q. (Max) (2005). Hydrothermal Synthesis of Layered Double Hydroxides (LDHs) from Mixed MgO and Al2O3: LDH Formation Mechanism. *Chemistry of Materials*, **17**, 1055–1062.

Yan L., Gonca S., Zhu G., Zhang W. and Chen X. (2019). Layered double hydroxide nanostructures and nanocomposites for biomedical applications. *Journal of Materials Chemistry B*, **7**, 5583–5601.

Zhao R., Yin C., Zhao H. and Liu C. (2003). Synthesis, characterization, and application of hydotalcites in hydrodesulfurization of FCC gasoline. *Fuel Processing Technology*, **81**, 201–209.